

# 3D Printing of Reduced Graphene Oxide Nanowires

Jung Hyun Kim, Won Suk Chang, Daeho Kim, Jong Ryul Yang, Joong Tark Han, Geon-Woong Lee, Ji Tae Kim, and Seung Kwon Seol\*

Graphene, a two-dimensional (2D) atomic layer of  $sp^2$ -hybridized carbon atoms densely packed in a honeycomb lattice, is the fundamental building block of all graphitic materials.<sup>[1,2]</sup> It has received a great deal of attention for its promising potential applications in electronics, biomedical and energy-storage devices, sensors, and other cutting-edge technological fields, mainly because of its fascinating properties such as extremely high electron mobility, good thermal conductivity, and high elasticity.<sup>[3–11]</sup> The successful implementation of graphene-based devices invariably requires the precise patterning of graphene sheets at both the micrometer and nanometer scales.<sup>[12]</sup> Finding the ideal technique to achieve the desired graphene patterning remains a major challenge.

A variety of chemical and physical techniques, including photolithography, soft-lithography, and direct writing, have been adapted to the patterning of graphene sheets. The photolithographic approaches,<sup>[13,14]</sup> which allow the removal of selected areas and the creation of precise and extensive patterns on the graphene sheets, have now reached a high level of maturity. However, they present some limitations, such as the need to employ additional etching processes, restrictions related to a limited choice of suitable substrates, and the high operating cost. On the other hand, soft-lithographic techniques such as microcontact printing ( $\mu$ CP), microtransfer molding ( $\mu$ TM), solvent-assisted micromolding (SAMIM), replica molding (REM), and micromolding in capillaries (MIMIC) allow the use of a broader range of materials as substrates,

offering at the same time simplicity and flexibility in creating specific patterns.<sup>[15–19]</sup> These techniques still present several issues to be faced, including the occurrence of deformations of the elastomeric stamp and a relatively high defect density in the resulting pattern. Non-lithographic approaches based on “direct writing” as an alternative to conventional lithography have also been tested, for instance dip-pen lithography and inkjet printing.<sup>[20–22]</sup> Direct-writing techniques provide a facile and practical process suitable for producing micro-patterned graphene sheets, providing high reliability and keeping the cost low. Most importantly, direct-writing patterning does not require the use of masks and photoresists. However, all of the above-mentioned techniques are limited to the patterning of two-dimensional or low-aspect-ratio structures of graphene, whereas for advanced applications three-dimensional (3D) patterning is essential.

Recently, the company Graphene 3D Lab has proposed a commercial plastic/graphene composite filament for 3D printing of graphene-enhanced plastic structures using a conventional fused deposition modeling (FDM) 3D printer. FDM, which is a representative material extrusion technique, is a 3D printing method based on heating up plastic materials and depositing them layer-by-layer through an extruder to create an object.<sup>[23–25]</sup> In such a composite system, graphene plays an important role in improving the properties of plastic materials currently used in 3D printers. However, the plastic materials used to produce the plastic/graphene composite deteriorate the intrinsic properties of graphene. Furthermore, the FDM method still suffers from the difficulty of downsizing printed structures to the nanometer scale. For the implementation of the next generation of graphene-based devices, 3D patterning of graphene nanostructures is a necessity. So far, to the best of our knowledge, nobody has reported 3D-printed nanostructures composed entirely of graphene.

In this Communication we describe a nanometer-scale 3D printing approach that exploits a size-controllable liquid meniscus to write freestanding reduced graphene oxide (rGO) nanowires without any supporting materials. Graphene oxide (GO) wires were locally grown at room temperature using the meniscus formed at the tip of a micropipette filled with a colloidal dispersion of GO sheets, then it was reduced by thermal or chemical treatment (with hydrazine). GO deposition was obtained by pulling the micropipette as the solvent rapidly evaporated, thus enabling the growth of GO wires. The rGO wire radius  $r$  was accurately controlled by tuning the pulling rate  $v$  of the pipette and could reach a minimum value of ca. 150 nm. We produced arrays of different freestanding rGO architectures: straight wires, bridges, suspended junctions, and woven structures. Each structure could be directly grown at the

J. H. Kim, W. S. Chang, Dr. D. Kim, Dr. J. T. Han,  
Dr. G.-W. Lee, Dr. S. K. Seol  
Nano Hybrid Technology Research Center  
Korea Electrotechnology Research  
Institute (KERI) Changwon-si  
Gyeongsangnam-do 642–120, Republic of Korea  
E-mail: skseol@keri.re.kr



Prof. J. T. Han, Prof. D. Kim, Prof. S. K. Seol  
Electrical Functional Material Engineering  
Korea University of Science and Technology  
Changwon-si, Gyeongsangnam-do 642–120, Republic of Korea

Dr. J. R. Yang  
Advanced Medical Device Research Center  
Korea Electrotechnology Research Institute (KERI)  
Ansan, Gyeonggi-do 426–910, Republic of Korea

Prof. J. T. Han, Prof. S. K. Seol  
Electrical Functional Material Engineering  
Korea University of Science and Technology  
Changwon-si, Gyeongsangnam-do 642–120, Republic of Korea

Dr. J. T. Kim  
Max Planck Institute for the Science of Light  
Günther-Scharowsky-Strasse 1/Bldg 24  
91058, Erlangen, Germany

DOI: 10.1002/adma.201404380

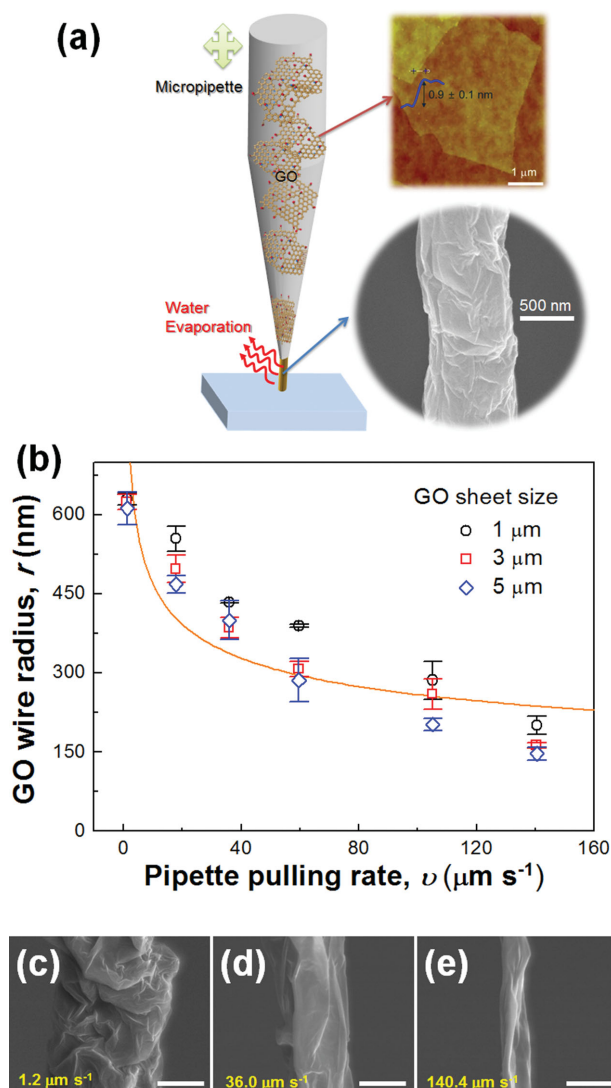


**Figure 1.** a) Schematic diagram of GO nanowire fabrication by pulling a micropipette filled with an aqueous GO suspension (GO sheet thickness =  $0.9 \pm 0.1$  nm) and stretching the meniscus during water evaporation. The nanowire radius  $r$  is controlled by pulling rate  $v$ . In the circle (lower right): FE-SEM image showing a grown rGO nanowire with  $r \approx 400$  nm. b) Plot of  $r$  versus  $v$  for a pipette opening of  $1.3 \mu\text{m}$  (GO sheet size = 1, 3, and  $5 \mu\text{m}$ ). The solid line corresponds to a functional dependence  $r \propto v^{-0.25}$ . c) FE-SEM images of freestanding rGO wires with different  $r$ , namely 625, 400, and 150 nm, corresponding to  $v = 1.2$ , 36.0, and  $140.4 \mu\text{m s}^{-1}$  respectively.

selected sites with an accuracy of 250 nm. In the present article, two applications for rGO nanowires fabricated with this novel methodology are described, namely, a stretchable interconnect for electronic devices and a transducer for gas sensors.

Figure 1a shows a schematic diagram of the 3D printing technique based on meniscus-guided growth.<sup>[26–28]</sup> To prepare the GO ink, GO sheets with a thickness of ca.  $0.9 \pm 0.1$  nm (see atomic force microscopy (AFM) height profile in Figure 1a) were well dispersed in water. GO is a layered material consisting of graphene sheets that have oxygen functional groups on their basal planes and edges. It can form colloidal dispersions

of single sheets in water and other polar organic solvents.<sup>[29]</sup> When the micropipette with  $1.3 \mu\text{m}$ -opening was moved close enough to the substrate, a meniscus of GO ink formed at its opening. As the micropipette was withdrawn, the meniscus stretched and its cross section decreased, reaching a size in the range of nanometers. During withdrawal of the micropipette, water evaporated rapidly from the nanometer-sized meniscus, allowing the formation of a freestanding GO nanowire (Movie S1, Supporting Information). It is reasonable that the faster evaporation of water molecules was induced by the very high surface-area-to-volume ratio reached in the nanometer-sized meniscus, leading to a massive increase in the area exposed to air. In order to understand GO wire formation in detail, we observed the flow and deposition of GO sheets in the meniscus (Movie S2, Supporting Information). For this observation, as an exception, the micropipette with  $2.6 \mu\text{m}$  opening was used, because of the limitation of optical image resolution. As the pipette is pulled away, the GO sheets flow down and converge at the opening of the pipette. We could clearly see that the GO sheets were deposited in the meniscus by their release at the pipette opening. The rGO nanowire shown in Figure 1a is characterized by a wrinkled surface and was obtained after reduction. Unlike in typical rGO fiber production, the use of coagulation agents was unnecessary because the GO nanowire remained coherent after complete evaporation of water, being held together by van der Waals forces.<sup>[30,31]</sup> These forces also clamped the GO sheets strongly to the substrate during the printing process.

Figure 1b shows schematically a strategy to control the nanowire radius  $r$ . Note that we were able to control the radius  $r$  of the grown rGO wires by carefully tuning the pulling rate  $v$  of the micropipette. The radius  $r$  is directly related to the pulling rate  $v$  and to the flow rate  $W$  of the GO solution though the pipette opening (ca.  $1.3 \mu\text{m}$ ), also a function of  $v$ . This radius-determination process could be described by the material balance law<sup>[32]</sup>

$$r = \left( \frac{W(v)}{\pi v} \right)^{1/2} \quad (1)$$

As shown in Figure 1b,  $r$  decreased from ca. 625 to ca. 150 nm as  $v$  increased from 1.2 to  $140.4 \mu\text{m s}^{-1}$ . The solid line in Figure 1b corresponds to the functional dependence  $r \propto v^{-0.25}$ . The flow rate  $W$  estimated using Equation (1), increases with  $W(v) \propto v^{-0.5}$ . The change of  $W$  with respect to  $v$  can be explained by the enhancement of the pressure on the GO solution.<sup>[33]</sup> This dependence of  $r$  on  $v$  was observed to remain constant when the average size of GO sheets dispersed in water varied between 1 and  $5 \mu\text{m}$  (Figure S1, Supporting Information). Interestingly, a decrease in the radius of the wires induced a change in their surface morphology. Figure 1c–e shows the surface morphology of wires grown at different  $v$ , namely 1.2, 36.0, and  $140.4 \mu\text{m s}^{-1}$ . Whereas the wires grown at  $v \approx 1.2 \mu\text{m s}^{-1}$ , with  $r \approx 625$  nm, do not show any kind of order in the stacking of the GO sheets, the morphology of wires with a reduced diameter (and grown at higher  $v$ , namely 36.0 and  $140.4 \mu\text{m s}^{-1}$ ) shows an alignment of GO sheets along the wire length. Such alignment, which is caused by the external shear forces applied during the pulling process, increases with

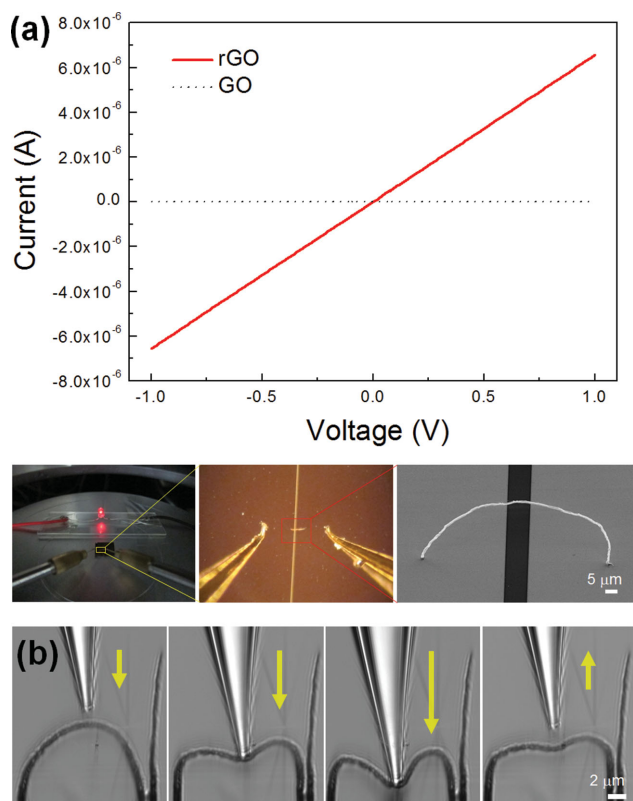


**Figure 2.** Electrical and mechanical properties of a typical rGO nanowire ( $r = 400$  nm). a)  $I$ - $V$  characteristics of an individual rGO nanowire (plot). The applied voltage ranged from  $-1.0$  to  $+1.0$  V in 20 mV steps. Optical and FE-SEM images show the rGO nanoarch between the gold electrodes with a  $10\ \mu\text{m}$  gap and the LED lamp switched on using the single rGO nanoarch as an electrical interconnect. b) Sequential optical images showing the bending of the rGO nanoarch.

decreasing wire diameter. It is worth noticing that a higher degree of alignment of GO sheets within the wires may provide a more efficient conductive path for electron conduction along the wire axis.<sup>[34]</sup>

The electrical and mechanical properties of rGO nanowires were also investigated. rGO nanoarches with  $r \approx 400$  nm were printed between gold electrodes separated by a gap of  $10\ \mu\text{m}$ . The effectiveness of the reduction of GO to rGO nanowires was confirmed by Raman spectrometry (Figure S2, Supporting Information). The value of the intensity ratio ( $I_D/I_G$ ) of the D band ( $1350\ \text{cm}^{-1}$ ) and G band ( $1585\ \text{cm}^{-1}$ ) characteristic of rGO wires is indicative of their degree of disorder, and the average size of the  $\text{sp}^2$  domains increases from 1.05 for GO wires to 1.43 for rGO wires. Findings are consistent with the literature, since an increase in the  $I_D/I_G$  ratio after reduction is commonly observed.<sup>[35]</sup> In Figure 2a (upper plot), the linear current-voltage ( $I$ - $V$ ) curve shows the presence of an ohmic contact between the rGO nanowire and the gold electrodes. The behavior of a non-conductive GO wire is shown for comparison (dotted line). Individual rGO nanowires had an electrical conductivity of ca.  $11.3\ \text{S cm}^{-1}$  at room temperature. It was also possible to switch on an LED lamp by using a single nanowire as an electrical connector between the gold electrodes, as shown in the photographs at the bottom of Figure 2a (and in Movies S3 and S4

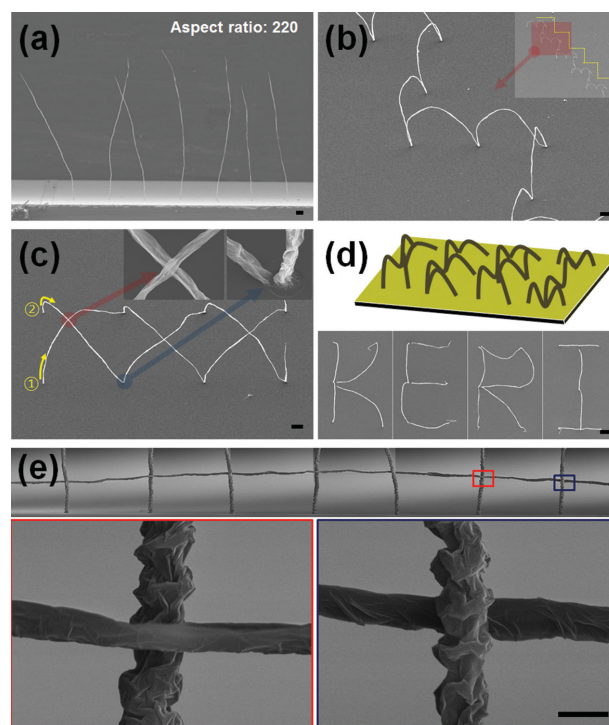


**Figure 3.** FE-SEM images of 3D printing of rGO nanowire architectures with different shapes and accurate positioning. a) An array of freestanding rGO nanowires ( $r = 400$  nm, aspect ratio = 220). b) A zigzag rGO nanoarch with a constant arch width ( $r = 400$  nm). c) A suspended rGO junction nanostructure assembled using two concatenated rGO nanoarches ( $r = 400$  nm). d) The word "KERI" made with nanoarches ( $r = 400$  nm). e) A woven structure consisting of a freestanding  $400\ \text{nm}$  radius rGO wire and several  $625\ \text{nm}$  radius rGO wires attached to the substrate (scale bar represents  $1\ \mu\text{m}$ ).

in the Supporting Information). Figure 2b presents sequential optical images showing the bending of a rGO nanoarch. The arch was pushed towards the substrate by a precisely controlled micropipette. When the central point of the arch contacted the substrate, the micropipette was moved upward and the original shape was restored (Movie S5, Supporting Information). This experiment highlights the stability and flexibility of the grown rGO nanowire.

Several different rGO wire architectures were successfully fabricated thanks to accurate control of the micropipette, demonstrating the ability of nanowires to grow in any direction and at any selected site. The field emission scanning electron microscopy (FE-SEM) image in Figure 3a shows an array of freestanding rGO nanowires with  $r \approx 400$  nm and an aspect ratio of 220. There is no evident limitation to the wire length  $L_w$  potentially achievable using the described technique. Figure 3b presents a zigzag structure consisting of concatenated rGO nanoarches with  $r \approx 400$  nm and constant arch width. Each nanoarch was fabricated in three steps: contacting, pulling, and attaching, as shown in Movie S6 (Supporting Information). A suspended rGO junction structure was also fabricated by assembling two concatenated rGO nanoarches with  $r \approx 400$  nm (Figure 3c). In Figure 3d, the FE-SEM images at the bottom are the top views of the letters of the word "KERI" fabricated using 21 rGO nanoarches with  $r \approx 400$  nm; the image



at the top is a schematic diagram describing the fabrication process. A further interesting architecture is the freestanding rGO woven structure shown in Figure 3e, realized by weaving a wire ( $r \approx 400$  nm), previously grown and detached from the substrate, with several vertical wires ( $r \approx 625$  nm) still attached to the substrate. Details at higher magnification are shown in the lower panels of Figure 3e.

rGO nanowires fabricated using the described 3D printing technique may be used as core components in a wide range of different devices. For example, the performance of rGO nanoarches as stretchable interconnects was tested for a wire with  $r \approx 400$  nm grown between gold electrodes with a variable gap  $L$ . A strain was applied by increasing  $L$  while measuring the wire's electrical resistance. Figure 4a shows the resistance as a function of the applied horizontal strain,  $\Delta L/L_0$ , when  $L_w$  and  $L_0$  were 310 and 30  $\mu\text{m}$ , respectively. The resistance shows a negligible variation for  $\Delta L/L_0$  up to 340%. Under applied strain  $\Delta L/L_0$ , the shape of rGO nanoarch changes in a manner that avoids substantial strains in the rGO wire itself.<sup>[36]</sup> The characteristics of the nanoarch remained invariant in the case of  $\Delta L/L_0 = 25\%$  or 150% for more than 120 stretching cycles. Findings show that rGO nanostructures like those presented here can be employed as flexible and stretchable components in 3D electronic devices.

We also demonstrated the use of rGO nanowires as 3D transducers in gas sensors. A prototype gas sensor was assembled by positioning five parallel rGO nanoarches with  $r \approx 400$  nm between two platinum electrodes separated by a 10  $\mu\text{m}$  gap. The performance of the transducer was characterized by measuring its electrical resistance upon exposure to  $\text{CO}_2$  at room temperature. Gas sensing basically depends on electron transfer reactions, which are redox reactions. The rGO is dominated by the presence of positively charged carriers (holes), whereas  $\text{CO}_2$  is mainly an electron donor.<sup>[37]</sup> Electron transfer from the adsorbed  $\text{CO}_2$  to rGO leads to a decrease in hole concentration, resulting in an increase of the electrical resistance of the nanoarches. Figure 4b shows the response of the transducer made from rGO nanoarches to a variation in  $\text{CO}_2$  concentrations between 0.25% and 5%. Though the sensitivity of the gas sensor demonstrated in this work was still low, the response was dependent on the  $\text{CO}_2$  concentration, and changes in the resistance were observed to be basically reversible at room temperature, except for a relatively low upward drift in the initial resistance  $R_0$ .

Our findings show that 3D printing of freestanding rGO nanowires can be realized at room temperature by local growth of GO at the meniscus formed at the tip of a micropipette and by the following reduction of GO by thermal or chemical treatment. By means of accurate control of the pipette, we successfully printed 3D rGO nanowires with diverse and complicated features, demonstrating their ability to grow in any direction and at the selected sites. The grown 3D rGO nanowires show ideal properties for the production of components in electrical devices such as stretchable interconnects and sensing transducers. We have presented here a few examples of various 3D integrated graphene nanowires with ca. 100 nm radius. Reducing the 3D printable size to below 10 nm still remains a challenge. To reduce the size of printed wires, a full characterization of the printing process described

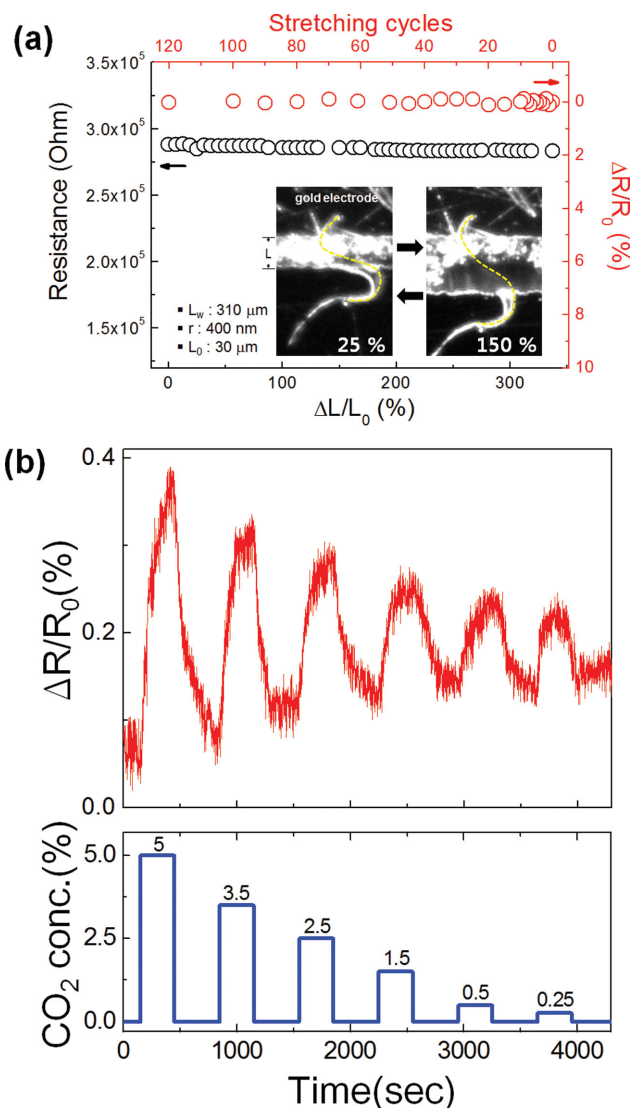


**Figure 4.** a) Resistance of the grown rGO nanowire ( $L_w = 310$   $\mu\text{m}$ ,  $r = 400$  nm, and  $L_0 = 30$   $\mu\text{m}$ ) as a function of strain ( $\Delta L/L_0$ ). The electrical resistance shows negligible variation during continuous stretching up to  $\Delta L/L_0 \approx 340\%$  (black circles) and repeated stretching between 25% and 150% over 120 cycles (red circles). The optical images in the inset show the condition of the nanowire at 25% and 150%  $\Delta L/L_0$ . b) Resistance change of the sensor assembled using five reduced rGO nanowires with time during exposure to  $\text{CO}_2$  between 0.25% and 5% at room temperature.

here is under way, for example in investigations of the graphene ink viscosity and the effects of the size of the pipette opening and the pulling rate. We are convinced that this novel approach is quite effective in 3D printing of graphene nanostructures for the implementation of the next generation of graphene-based devices.

## Experimental Section

**3D Printing of Reduced Graphene Oxide (rGO) Nanowires:** 3D rGO structures were fabricated at the meniscus formed at the tip of a micropipette filled with an aqueous suspension of GO sheets ( $1 \text{ g L}^{-1}$ )

with an average size of 1, 3, or 5  $\mu\text{m}$ . GO was prepared from natural graphite (Alfa Aesar, 99.999% purity,  $-200$  mesh) by a modified Hummers method. Briefly, graphite (20 g) and  $\text{H}_2\text{SO}_4$  (460 mL) were mixed in a flask. Then  $\text{KMnO}_4$  (60 g) was slowly added over 1 h in an ice-water bath. After the mixture had been stirred vigorously for 3 days at room temperature, deionized water (920 mL) was added, before the mixture was stirred again for 10 min in an ice-water bath.  $\text{H}_2\text{O}_2$  (50 mL of 30 wt% aqueous solution) was then added, and the mixture was stirred for 2 h at room temperature. The resulting mixture was centrifuged at 10000 rpm for 1 h to obtain the graphite oxide powder. Exfoliation of graphite oxide to GO was accomplished by ultrasonication of the yellow-brown graphite oxide solution.

All the results presented and discussed here refer to nanowires prepared using GO sheets with a size of 5  $\mu\text{m}$ , except for the plot of  $r$  versus  $v$ , for which GO sheets of all the available sizes were used. Atomic force microscopy (AFM) images of GO sheets were acquired in tapping mode using a sample prepared by spin-coating a GO suspension at 1000 rpm. Glass micropipettes with opening diameters of about 1.3 and 2.6  $\mu\text{m}$  were obtained using a pipette puller (P-97, Sutter Instrument). The opening diameters of the pipettes were set as 1.3  $\mu\text{m}$  for all results discussed here, except in the case of observation of GO sheet deposition in the meniscus. The GO ink was introduced at the back of the micropipette and drawn to the front tip by capillary forces without any applied pressure. The position and pulling rate of the micropipette during nanowire fabrication were accurately controlled by three-axis stepping motors with a positioning accuracy of 250 nm. The growth process was observed in situ using a high-resolution monitoring system consisting of an optical lens and a charge-coupled device camera (Spot RT Xplore). Gold-coated silicon wafers were used as substrates for freestanding GO structures, movable gold-coated electrodes with 30  $\mu\text{m}$  gaps fabricated on poly(dimethylsiloxane) (PDMS) were used for the stretchable interconnects, and plates covered with platinum patterns with 10  $\mu\text{m}$  gaps were used for the gas-sensing transducers. As-grown GO wires were reduced to rGO nanowires by a thermal treatment performed at 400  $^\circ\text{C}$  for 1 h in vacuum. For the stretchable interconnect, chemical reduction with hydrazine (at 120  $^\circ\text{C}$  for 12 h) was preferred because the PDMS substrate would have been damaged by the thermal treatment.

**rGO Nanowire Characterization:** The microscopic characteristics of the nanowires were analyzed using FE-SEM (Hitachi S-4800). The structural changes taking place following the reduction of GO to rGO were examined using a Raman spectroscope (NTEGRA Spectra) with a 532 nm laser. Current–voltage ( $I$ – $V$ ) characteristics of individual rGO nanowires were measured using a two-probe method with a Keithley 2612A instrument at room temperature. The sensor produced by printing rGO nanowires on two platinum-coated silicon electrodes with a 10  $\mu\text{m}$  gap was tested at room temperature. Pb wires attached to the electrodes with silver paste were used to obtain an electrical connection with the measurement system. The sensor was placed in a home-made chamber with inlet and outlet pipes for gas flow. Mass flow controllers (Mykrolis FC-280C) were used to regulate the nitrogen (99.999% purity) and carbon dioxide ( $\text{CO}_2$ ) gas flows. The concentration of  $\text{CO}_2$  was varied between 0.25% and 5% by adjusting the  $\text{CO}_2$  and nitrogen rates. Pure nitrogen was used to purge the system from any residual  $\text{CO}_2$  and allowed the resistance of the sensor to return to the baseline condition  $R_0$ , although with a relatively small upward drift. The sensor response was defined as  $\Delta R/R_0$  (%), where  $R_0$  is the resistance of the arched wire before exposure to  $\text{CO}_2$  and  $\Delta R$  is the change in resistance induced by exposure to  $\text{CO}_2$ . The electrical resistance of the sensor was measured under a bias voltage of 0.5 V using a sourcemeter (Keithley 2612A).

## Supporting Information

Supporting Information is available from the Wiley Online Library or from the author.

## Acknowledgements

We gratefully acknowledge the financial support provided in the form of a grant from the Primary Research Program of Korea Electrotechnology Research Institute (KERI), Republic of Korea.

Received: September 23, 2014

Published online:

- [1] K. S. Novoselov, A. K. Geim, S. V. Morozov, D. Jiang, Y. Zhang, S. V. Dubonos, I. V. Grigorieva, A. A. Firsov, *Science* **2004**, *306*, 666.
- [2] A. K. Geim, K. S. Novoselov, *Nat. Mater.* **2007**, *6*, 183.
- [3] A. K. Geim, *Science* **2009**, *324*, 1530.
- [4] M. D. Stoller, S. J. Park, Y. W. Zhu, J. H. An, R. S. Ruoff, *Nano Lett.* **2008**, *8*, 3498.
- [5] S. Han, D. Wu, S. Li, F. Zhang, X. Feng, *Small* **2013**, *9*, 1173.
- [6] S. Mao, G. Lu, K. Yu, Z. Bo, J. Chen, *Adv. Mater.* **2010**, *22*, 3521.
- [7] S. Myung, A. Solanki, C. Kim, J. Park, K. S. Kim, K. B. Lee, *Adv. Mater.* **2011**, *23*, 2221.
- [8] J. T. Robinson, F. K. Perkins, E. S. Snow, Z. Q. Wei, P. E. Sheehan, *Nano Lett.* **2008**, *8*, 3137.
- [9] K. P. Loh, Q. Bao, G. Eda, M. Chhowalla, *Nat. Chem.* **2010**, *2*, 1015.
- [10] S. B. Kumar, J. Gao, *Nano Lett.* **2012**, *12*, 1362.
- [11] M. L. Hammock, A. Chortos, *Adv. Mater.* **2013**, *25*, 5997.
- [12] Y. Zhou, K. P. Loh, *Adv. Mater.* **2010**, *22*, 3615.
- [13] M. Geissler, Y. Xia, *Adv. Mater.* **2004**, *16*, 1249.
- [14] S. Pang, H. N. Tsao, X. Feng, K. Müllen, *Adv. Mater.* **2009**, *21*, 3488.
- [15] Z. Wei, D. E. Barlow, P. E. Sheehan, *Nano Lett.* **2008**, *8*, 3141.
- [16] S. H. Hur, D. Y. Khang, C. Kocabas, J. A. Rogers, *Appl. Phys. Lett.* **2004**, *85*, 5730.
- [17] M. L. Chabiny, A. Salleo, Y. Wu, P. Liu, B. S. Ong, M. Heeney, I. McCulloch, *J. Am. Chem. Soc.* **2004**, *126*, 13928.
- [18] B. Li, G. Lu, X. Zhou, X. Cao, F. Boey, H. Zhang, *Langmuir* **2009**, *25*, 10455.
- [19] M. Xue, F. Li, J. Zhu, H. Song, M. Zhang, T. Cao, *Adv. Funct. Mater.* **2012**, *22*, 1284.
- [20] R. J. Stohr, R. Kolesov, K. Xia, J. Wrachtrup, *ACS Nano* **2011**, *5*, 5141.
- [21] K. Salata, Y. H. Wang, C. A. Mirkin, *Nat. Nanotechnol.* **2007**, *2*, 145.
- [22] K. Y. Shin, J. Y. Hong, J. Jang, *Adv. Mater.* **2011**, *23*, 2113.
- [23] Z. Iwan, H. W. Dietmar, C. T. Kim, H. T. Swee, *Biomaterials* **2002**, *23*, 1169.
- [24] P. M. Pandey, N. V. Reddy, S. G. Dhande, *J. Mater. Process. Technol.* **2003**, *132*, 323.
- [25] S. H. Masood, W. Q. Song, *Mater. Des.* **2004**, *25*, 587.
- [26] J. T. Kim, S. K. Seol, J. Pyo, J. S. Lee, J. H. Je, G. Margaritondo, *Adv. Mater.* **2011**, *23*, 1968.
- [27] S. K. Seol, W. S. Chang, D. Kim, S. Jung, *RSC Adv.* **2012**, *2*, 8926.
- [28] W. S. Chang, J. H. Kim, D. Kim, S. H. Cho, S. K. Seol, *Macromol. Chem. Phys.* **2014**, *215*, 1633.
- [29] D. A. Dikin, S. Stankovich, E. J. Zimney, R. D. Piner, G. H. B. Dommett, G. Evmenenko, S. T. Nguyen, R. S. Ruoff, *Nature* **2007**, *448*, 457.
- [30] H. P. Cong, X. C. Ren, P. Wang, S. H. Yu, *Sci. Rep.* **2012**, *2*, 613.
- [31] Z. Dong, C. Jiang, H. Cheng, Y. Zhao, G. Shi, L. Jiang, L. Qu, *Adv. Mater.* **2012**, *24*, 1856.
- [32] Z. Gou, A. J. McHugh, *J. Non-Newtonian Fluid Mech.* **2004**, *118*, 121.
- [33] R. B. Bird, W. E. Stewart, E. N. Lightfoot, *Transport Phenomena*, 2nd ed., Wiley, New York **2007**.
- [34] L. Chen, Y. He, S. Chai, H. Qiang, F. Chen, Q. Fu, *Nanoscale* **2013**, *5*, 5809.
- [35] V. Strong, S. Dubin, M. F. El-Kady, A. Lech, Y. Wang, B. H. Weiller, R. B. Kaner, *ACS Nano* **2012**, *6*, 1395.
- [36] D. H. Kim, J. A. Rogers, *Adv. Mater.* **2008**, *20*, 4887.
- [37] J. E. Fowler, M. J. Allen, V. C. Tung, Y. Yang, R. B. Kaner, B. H. Weiller, *ACS Nano* **2009**, *3*, 301.